



# Extended H-bonds/ $\pi$ -bonds networks for boosting electron transfer over polydopamine-covered nanocellulose/g-C<sub>3</sub>N<sub>4</sub> toward efficient photocatalytic H<sub>2</sub>O<sub>2</sub> production

Tianshang Shan<sup>a,b</sup>, Yu Wang<sup>a,b</sup>, Dan Luo<sup>a,b</sup>, Zhichun Huang<sup>a,b</sup>, Fengshan Zhang<sup>c</sup>, Hui Wu<sup>a,b</sup>, Liulian Huang<sup>a,b</sup>, Jingde Li<sup>d,\*</sup>, Lihui Chen<sup>a,b</sup>, He Xiao<sup>a,b,c,\*\*</sup>

<sup>a</sup> College of Material Engineering, Fujian Agriculture and Forestry University, Fuzhou, Fujian 350108, China

<sup>b</sup> National Forestry and Grassland Administration Key Laboratory of Plant Fiber Functional Materials, Fuzhou, Fujian 350108, China

<sup>c</sup> Shandong Huatai Paper Co., Ltd. & Shandong Yellow Triangle Biotechnology Industry Research Institute Co. Ltd., Dongying 257335, China

<sup>d</sup> School of Chemical Engineering and Technology, Hebei University of Technology, Tianjin 300130, China

## ARTICLE INFO

### Keywords:

Graphitic carbon nitride  
Cellulose nanofibers  
Polydopamine  
Hydrogen peroxide  
Intermolecular interactions

## ABSTRACT

Photocatalytic hydrogen peroxide production (PHP) from H<sub>2</sub>O and O<sub>2</sub> is a promising solar-to-chemical conversion technology. However, conventional doping, heterojunction and defect engineering of catalyst modification for enhanced PHP process is unable to meet the highly requirements of efficient oxygen reduction reaction (ORR), while also damaging the intrinsic crystal structure of the catalysts. Herein, we demonstrate a rationally extended H-bonds/ $\pi$ -bonds intermolecular networks between carbon nitride (g-C<sub>3</sub>N<sub>4</sub>, CN) and carboxylated cellulose nanofibers (CNF) with a small quantity of polydopamine (PDA) for solar H<sub>2</sub>O<sub>2</sub> production. Ultimately, CN/CNF<sub>p</sub> exhibits an extraordinary PHP of 130.7  $\mu\text{mol}\cdot\text{L}^{-1}\cdot\text{h}^{-1}$ , surpassing CN/CNF (75.2  $\mu\text{mol}\cdot\text{L}^{-1}\cdot\text{h}^{-1}$ ) and pure CN (20.1  $\mu\text{mol}\cdot\text{L}^{-1}\cdot\text{h}^{-1}$ ). Experimental and density function theory (DFT) have validated that CNF<sub>p</sub> increases the adsorption capabilities of O<sub>2</sub>, enhancing the efficiency of photogenerated charge transfer and separation via multiple hydrogen bonding/ $\pi$ - $\pi$  stacking with g-C<sub>3</sub>N<sub>4</sub>, thereby facilitating the superior PHP via a two-step single-electron ORR pathway. This work offered a viable route to modulate directed transfer of photo-generated charges with multiple intermolecular interactions and presented an encouraging strategy to obtain high-efficient PHP.

## 1. Introduction

Hydrogen peroxide (H<sub>2</sub>O<sub>2</sub>), as a green oxidizing agent [1], is widely used in industries such as pulp bleaching [2], pharmaceuticals [3], and water treatment [4] due to its decomposition into H<sub>2</sub>O and O<sub>2</sub>, which does not pose a threat to the environment. Currently, the anthraquinone method [5] is the main synthetic approach for H<sub>2</sub>O<sub>2</sub>, accounting for over 90% of the total production, but suffering drawbacks like high energy consumption and severe environmental pollution. At this point, photocatalytic H<sub>2</sub>O<sub>2</sub> production (PHP) [6], only using light, O<sub>2</sub>, H<sub>2</sub>O, and photocatalysts as reactants, possesses strong competitiveness among all the H<sub>2</sub>O<sub>2</sub> production methods [7,8]. Hence, selecting an appropriate photocatalyst is essential to the construction of photocatalytic system.

Graphitic carbon nitride (g-C<sub>3</sub>N<sub>4</sub>) [9–11], as a non-metal and

low-cost photocatalyst, has suitable energy band structures to harness photogenerated carriers for PHP. However, the capabilities of g-C<sub>3</sub>N<sub>4</sub> is significantly hindered by limitations in rapid recombination and slow transfer of electron (e<sup>-</sup>)-hole (h<sup>+</sup>) pairs, as well as poor absorption of light and O<sub>2</sub> [12]. Up till now, researchers have targeted the drawbacks of g-C<sub>3</sub>N<sub>4</sub> and made significant progress by employing various strategies, such as adding sacrificial agents [13], constructing homojunctions [14]/heterojunctions [11,15–17], doping elements [18–21], and introducing carbon/nitrogen vacancies [22–24]. Nevertheless, the predominant emphasis of these strategies lies in strong interactions (covalent bond, ionic bond, etc.), while research on weak interactions (hydrogen bond [25], van der Waals force [26], and electronic interaction [27]) remain limited. Based on current reports, the preparation strategies of weak interactions just require mild reaction conditions and cause no

\* Corresponding author.

\*\* Corresponding author at: College of Material Engineering, Fujian Agriculture and Forestry University, Fuzhou, Fujian 350108, China.

E-mail addresses: [cnjingdeli@hebut.edu.cn](mailto:cjnjingdeli@hebut.edu.cn) (J. Li), [xiaohex\\_river@163.com](mailto:xiaohex_river@163.com) (H. Xiao).

<https://doi.org/10.1016/j.apcatb.2024.123872>

Received 9 January 2024; Received in revised form 13 February 2024; Accepted 21 February 2024

Available online 22 February 2024

0926-3373/© 2024 Elsevier B.V. All rights reserved.

damage to the g-C<sub>3</sub>N<sub>4</sub> surface. Furthermore, the photocatalysts can be readily acquired by physical stirring, making this approach highly promising for further exploration. Given our prior work, carboxymethyl cellulose (CMC) with varying degrees of substitution was employed to composite with g-C<sub>3</sub>N<sub>4</sub> [28]. By means of experimental analysis and DFT calculations, the elucidation of how hydrogen bonding strength affects the PHP performance of the photocatalysts has been achieved. While further investigations into the synergistic effects of hydrogen bonding and  $\pi$ - $\pi$  stacking for enhanced PHP have not been extensively studied.

Carboxylated cellulose nanofibers (CNF) [29], as a fibrous nanomaterial (diameter: <50 nm, length: 1–3  $\mu$ m), possesses advantages such as wide accessibility, excellent dispersibility, and simple functional modification, which is extensively utilized in facial masks making [30], plastic synthesis [31], and food packaging [32]. With its abundant carboxyl and hydroxyl groups (-COOH/-OH), CNF can form hydrogen bonding self-assemblies with the amino groups (-NH<sub>2</sub>) of g-C<sub>3</sub>N<sub>4</sub>. On this basis, polydopamine (PDA) [33] with phenolic structures and can establish hydrogen bonding interactions with CNF and undertake  $\pi$ - $\pi$  stacking with CN, facilitating the investigation of the mechanism of synergistic effects arising from various weak interactions on PHP. Furthermore, PDA, as a novel black biomimetic material, possesses notable attributes, including efficient light absorption, robust adhesion, and facile synthetic procedures, rendering it highly suitable for applications in the realm of photocatalysis [34].

Thus, we have developed an easy method for preparing g-C<sub>3</sub>N<sub>4</sub>-based photocatalysts incorporating multiple weak intermolecular interactions via introducing phenolic PDA and -COOH/-OH-rich cellulose nanofibers (CNF). PDA enhances the O<sub>2</sub> adsorption and facilitates the charge separation/transfer in CN/CNF<sub>P</sub>. The density function theory (DFT) reveals that the  $\pi$ - $\pi$  stacking between PDA and CN, as well as the hydrogen bonding interactions between CNF and CN, synergistically promote the PHP performance of CN/CNF<sub>P</sub>, which exhibits 130.7  $\mu$ mol·L<sup>-1</sup>·h<sup>-1</sup>, nearly 1.7 times superior to CN/CNF (75.2  $\mu$ mol·L<sup>-1</sup>·h<sup>-1</sup>), and 6.5 times that of CN (20.1  $\mu$ mol·L<sup>-1</sup>·h<sup>-1</sup>). This work provides novel insights into the mechanistic influence of synergistic effects arising from multiple weak intermolecular interactions on PHP of g-C<sub>3</sub>N<sub>4</sub>-based photocatalysts.

## 2. Experimental

### 2.1. Preparation of CN

Typically, melamine (1 g) and cyanuric acid (1 g) were individually dissolved in 70 mL of water at 80°C with stirring (500 rpm·min<sup>-1</sup>) until complete dissolution. Then, the solutions were transferred to a 200 mL round flask and stirred (500 rpm·min<sup>-1</sup>) at 120°C for 12 h, with a temperature increase of 4°C per minute. Next, the supramolecular self-assemblies were washed with water at 80°C for 3–5 times and vacuum-dried at 60°C for 12 h. Subsequently, the white powder was transferred to an alumina crucible (covered with a lid) and underwent calcination in a tube furnace at 520°C for 2 h, with a temperature increase of 5°C per minute. Finally, the obtained yellow powder was thoroughly ground and designated as CN.

### 2.2. Preparation of CN/CNF

CN (2 g) was dispersed in 50 mL of varying mass ratio of CNF and stirred for 24 h. Then, the mixture was vacuum-dried at 60°C for 12 h, yielding a light-yellow powder. Next, the resulting samples were thoroughly ground and identified as CN/CNF<sub>x</sub>, where x (1%, 5%, 10%, 20%) represents the mass percentage of CNF in CN. Specifically, the sample with a mass percentage of 10% CNF was designated as CN/CNF.

### 2.3. Preparation of CN/CNF<sub>P</sub>

CNF (0.2 g) and varying mass ratio of dopamine (DA) were dispersed

in 50 mL of 0.02 mM Tris-HCl buffer solution (pH=8.5) and stirred for 12 h. Subsequently, CN (2 g) was added to the suspension and stirred for 12 h. Following that, multiple washing steps were carried out by ethanol until a neutral pH of 7 was attained. After vacuum-drying at 60°C for 12 h and thorough grinding, a gray powder was obtained, and it was designated as CN/CNF<sub>P-y</sub>, where y (0.01%, 0.05%, 0.1%, 0.5%, and 1%) represents the mass percentage of PDA in CN, with the optimal composition of CN/CNF<sub>P-0.1%</sub> referred to as CN/CNF<sub>P</sub> (Fig. 1).

### 2.4. Preparation of CNF<sub>P</sub>

CNF (0.2 g) and DA (2 mg) were dispersed in 50 mL of 0.02 mM Tris-HCl buffer solution (pH=8.5) and stirred for 24 h. Following that, multiple washing steps were carried out by ethanol until a neutral pH of 7 was attained. After vacuum-drying at 60°C for 12 h and thorough grinding, a gray powder was obtained, and it was designated as CNF<sub>P</sub>.

### 2.5. Experiment of photocatalysis

Typically, a 25 mg sample was dispersed in 25 mL of water, after 5 min of sonication, and then underwent continuous purging with O<sub>2</sub> (0.5 L·min<sup>-1</sup>) while being stirred at 100 rpm in dark for 30 min to achieve the adsorption-desorption equilibrium. Next, the suspension was irradiated from a 300 W Xenon lamp ( $\lambda \geq 420$  nm) and stirred at 100 rpm·min<sup>-1</sup> for 1 h. The lamp was positioned 10 cm away from the suspension, and the light intensity was set at 10 mW·cm<sup>-2</sup>. Subsequently, at 15 min intervals, 3 mL of the suspension was withdrawn and filtered using a membrane (0.22  $\mu$ m). Furthermore, to assess the stability of the catalysts, the solid samples were retrieved through centrifugation and re-dispersed under identical conditions for the following cycles. Additionally, in order to examine the photocatalytic decomposition of H<sub>2</sub>O<sub>2</sub>, 25 mg of the samples were added to a 1 mM aqueous solution of H<sub>2</sub>O<sub>2</sub> (25 mL) and exposed to visible light for 1 h, alongside continuous argon flow and magnetic stirring (100 rpm·min<sup>-1</sup>). Similarly, 3 mL of the suspension was sampled every 15 min and fully filtered. The concentration of H<sub>2</sub>O<sub>2</sub> was determined using the colorimetric N, N-diethyl-phenylenediamine (DPD) method, described in previous studies [35, 36]. Finally, the mixture was agitated for 30 s and subjected to analysis using UV-visible spectrophotometry at a wavelength of 551 nm. Besides, 1 mM p-benzoquinone (PBQ, ·O<sub>2</sub><sup>-</sup>), 0.5 mM AgNO<sub>3</sub> (e<sup>-</sup>), and 1 mM EDTA-2Na (h<sup>+</sup>) were used as different scavengers. The detailed description of the photocatalytic reaction system and the H<sub>2</sub>O<sub>2</sub> calibration curve can be found in Fig. S1, S2, respectively.

## 3. Results and discussion

### 3.1. Characterization of photocatalysts

Firstly, the chemical structures of PDA, CNF, and CNF<sub>P</sub> were gained via Fourier-transform infrared (FT-IR) spectroscopy and transmission electron microscopy (TEM). From Fig. 2a, it can be observed that the functional groups of PDA are mainly located at 3203 cm<sup>-1</sup>, 1603 cm<sup>-1</sup>, and 1505 cm<sup>-1</sup>, corresponding to -O-H, -N-H, and -C=C functional groups, respectively [37,38]. And the FT-IR peaks of CNF at 3357 cm<sup>-1</sup>, 2874 cm<sup>-1</sup>, and 1585 cm<sup>-1</sup> attribute to -O-H, -C-H, and -C=O, separately [39,40]. The obtained CNF<sub>P</sub> is demonstrated by the concurrent presence of -O-H and -C=C functional group peaks of PDA at 3203 cm<sup>-1</sup> and 1505 cm<sup>-1</sup>, as well as -O-H, -C-H, and -C=O functional group peaks of CNF at 3357 cm<sup>-1</sup>, 2874 cm<sup>-1</sup>, and 1585 cm<sup>-1</sup>, respectively. Fig. 2b-c shows the TEM image and element mapping analysis taken from CNF<sub>P</sub>, making clear that CNF exhibits an interconnected fibrous morphology (diameter: <50 nm, length: 1–3  $\mu$ m) covered with PDA nanoparticles (diameter: ~200 nm) and CNF<sub>P</sub> contains a significant amount of carbon (C), nitrogen (N), and oxygen (O) elements. These characterizations jointly confirm the successful preparation of CNF<sub>P</sub>.

The crystal structure and functional groups of different samples were

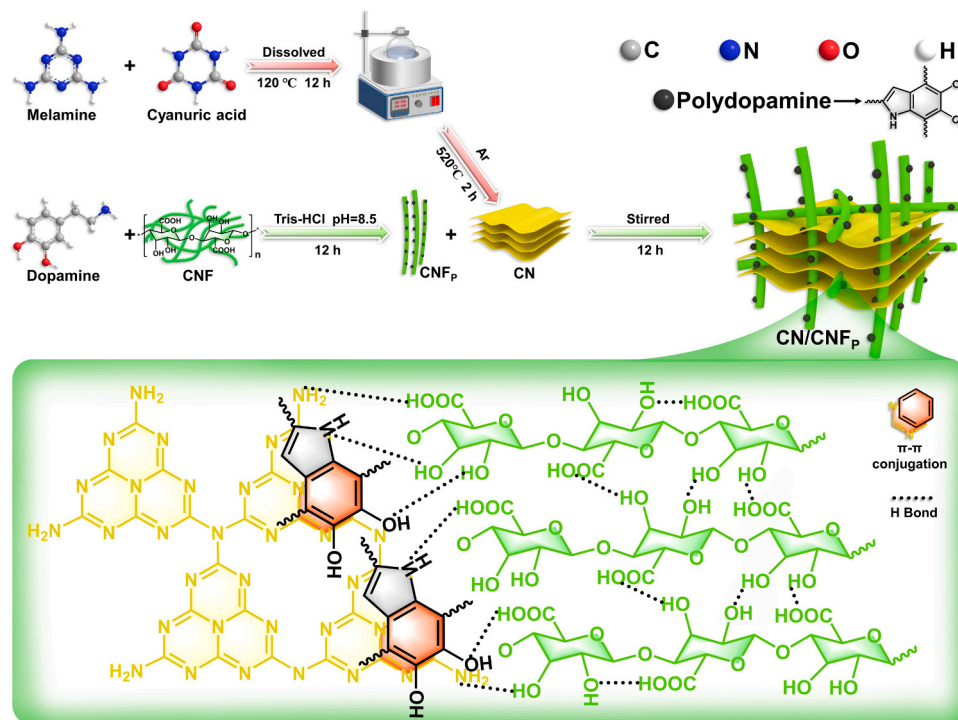


Fig. 1. Schematics of the synthesis process of CN/CNF<sub>p</sub> photocatalyst.

characterized using X-ray diffraction (XRD) and FT-IR spectroscopy. As shown in Fig. S3 and Fig. 2d, CNF illustrates strong peaks at  $16^\circ$ ,  $22^\circ$ , and  $35^\circ$ , matching with the (110), (200), and (004) crystal planes originated from the type I $\beta$  lattice diffraction [41,42]. PDA shows weak broad peaks at  $15^\circ$ – $35^\circ$ , corresponding to its low crystallinity [43]. At the same time, CN, CN/CNF, and CN/CNF<sub>p</sub> photocatalysts exhibit similar characterization peaks at  $13.1^\circ$  and  $27.4^\circ$ , in line with the (100) and (002) crystal planes formed by the periodic arrangement of tri-s-triazine rings and the interlayer stacking of aromatic structures, respectively [44,45]. Nevertheless, in CN/CNF and CN/CNF<sub>p</sub> samples, the absence of peaks for CNF and PDA can be attributed to the low content. Besides, the peak of (002) crystal plane for CN, CN/CNF, and CN/CNF<sub>p</sub> photocatalysts show a slight increase in angle (from  $27.38^\circ$  to  $27.43^\circ$ ) and intensity, indicating that CNF and PDA have influenced the interlayer spacing of g-C<sub>3</sub>N<sub>4</sub>. Fig. 2e presents the FT-IR spectra of CN, CN/CNF, and CN/CNF<sub>p</sub> which illustrate similar functional groups at  $810\text{ cm}^{-1}$ ,  $1200$ – $1700\text{ cm}^{-1}$ , and  $3000$ – $3400\text{ cm}^{-1}$ , in correspondence with the vibration characteristic peaks of tri-s-triazine units, g-C<sub>3</sub>N<sub>4</sub> cycle, and -NH<sub>2</sub>, respectively [46,47]. This outcome with the absence of FT-IR peak of CNF and PDA might be a result of insufficient amounts of CNF and PDA consistent with the XRD results. As depicted in Fig. 2f, the thermogravimetric analysis (TGA) curves of CN/CNF and CN/CNF<sub>p</sub> exhibit significant weight loss between  $250 \sim 500^\circ\text{C}$ , attributed to the decomposition of CNF. Meanwhile, the derivative thermogravimetry (DTG) curves show an increase of the maximum decomposition temperatures for CN ( $685^\circ\text{C}$ ), CN/CNF ( $690^\circ\text{C}$ ), and CN/CNF<sub>p</sub> ( $700^\circ\text{C}$ ), indicating that CNF and PDA changed the thermal stability of CN.

The microstructure and morphology of different photocatalysts were analyzed using SEM and TEM. The CN (Fig. 2g) sample exhibits a regular layered structure with a smooth surface. Besides, it can be seen in CN/CNF (Fig. 2h) and CN/CNF<sub>p</sub> (Fig. 2i) photocatalysts that fibrous CNF have interspersed between the CN layers. Fig. S4 showcases the TEM mapping results of CN/CNF<sub>p</sub>, evidencing the homogeneous dispersion of C, O, and N elements across the sample. In specific, the O element is possibly sourced from CNF and PDA. This conjecture further proved by the XPS elemental analysis (Table S1) in each sample (O element: CN (0.7%) < CN/CNF (20.7%) < CN/CNF<sub>p</sub> (21.6%), O/C: CN (0.01) < CN/

CNF<sub>p</sub> (0.42) < CN/CNF (0.46)). The N<sub>2</sub> adsorption/desorption isotherms and pore size distribution of the photocatalysts are displayed in Fig. S5a, b. There is minimal change in the specific surface area for CN ( $37.79\text{ m}^2\cdot\text{g}^{-1}$ ), CN/CNF ( $33.77\text{ m}^2\cdot\text{g}^{-1}$ ), and CN/CNF<sub>p</sub> ( $41.38\text{ m}^2\cdot\text{g}^{-1}$ ). In addition, the average pore width among the three samples are as follows: CN ( $25.91\text{ nm}$ ) > CN/CNF ( $24.49\text{ nm}$ ) > CN/CNF<sub>p</sub> ( $22.64\text{ nm}$ ). This variation could potentially be attributed to the structural modulation of CN induced by the introduction of CNF and PDA. In conclusion, the aforementioned characterizations provide evidence for the successful preparation of CN, CN/CNF, and CN/CNF<sub>p</sub> samples.

### 3.2. Photocatalytic performance on H<sub>2</sub>O<sub>2</sub> synthesis

As illustrated in Fig. 3a-c, the optimized CN/CNF exhibits excellent photocatalytic H<sub>2</sub>O<sub>2</sub> production (PHP) of  $75.2\text{ }\mu\text{mol}\cdot\text{L}^{-1}\cdot\text{h}^{-1}$ . Upon further addition of an optimal amount of PDA with CNF, the PHP of CN/CNF<sub>p</sub> achieves a remarkable performance of  $130.7\text{ }\mu\text{mol}\cdot\text{L}^{-1}\cdot\text{h}^{-1}$ , which exhibits a magnitude 6.5-fold increase compared to pure CN of  $20.1\text{ }\mu\text{mol}\cdot\text{L}^{-1}\cdot\text{h}^{-1}$ . Furthermore, the AQE (Fig. 3d) of PHP was obtained at different wavelength (400, 420, 450, 500, 550 nm) for 1 h and the calculated equation is shown in supporting information. As the calculated results, the AQE of CN/CNF<sub>p</sub> reaches superior 3% at 400 nm and 1.8% at 420 nm. And Fig. 3e illustrates that the SCC efficiency (calculation formula is illustrated in supporting information) of CN/CNF<sub>p</sub> reached as high as 0.101%, which was 6.5 times of the CN (0.018%) and 1.73 times of the CN/CNF (0.066%). The XRD patterns (Fig. 3f) of the three samples before and after 5 times of reaction remain almost unchanged, demonstrating the stability of the prepared photocatalysts over extended periods of use. In addition, the PHP reusability of photocatalysts were shown in Fig. S6. Besides, Fig. 3g and Fig. 3h present the H<sub>2</sub>O<sub>2</sub> photodegradation and the K<sub>f</sub>-K<sub>d</sub> plot for the three samples, respectively. In specific, CN/CNF<sub>p</sub> exhibits the least photodegradation of H<sub>2</sub>O<sub>2</sub>. Moreover, compared to the K<sub>f</sub> value ( $22.3\text{ }\mu\text{mol}\cdot\text{L}^{-1}\cdot\text{h}^{-1}$ ) and K<sub>d</sub> value ( $0.20\text{ h}^{-1}$ ) of CN, the K<sub>f</sub> value and K<sub>d</sub> value of CN/CNF<sub>p</sub> achieves a significant increase to  $136\text{ }\mu\text{mol}\cdot\text{L}^{-1}\cdot\text{h}^{-1}$  and  $0.09\text{ h}^{-1}$ , respectively. These results can be attributed to the synergistic effects of CNF and PDA. In the end, the CN/CNF<sub>p</sub> exhibits the excellent ability of PHP, which was



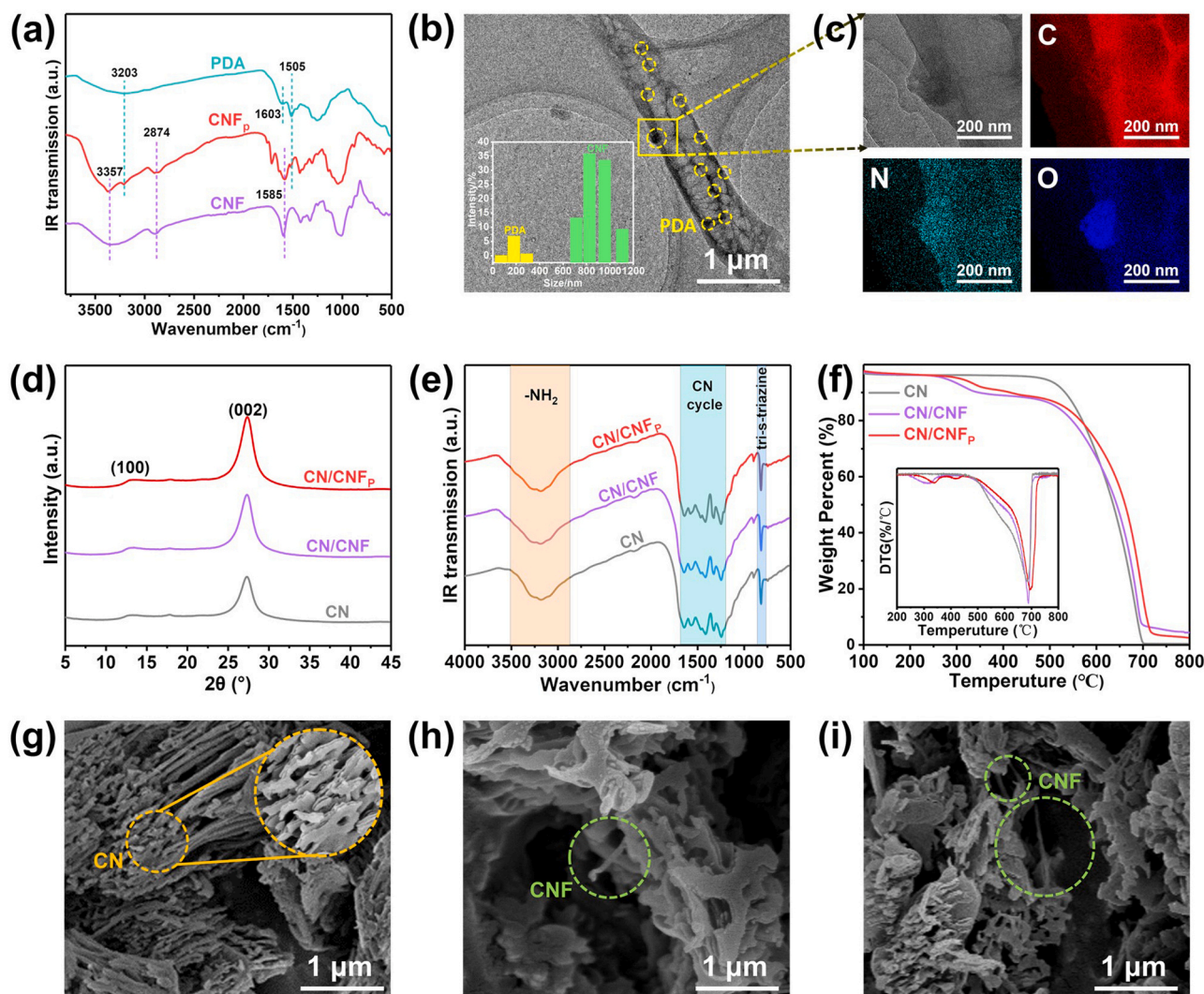


**Fig. 2.** (a) FT-IR plots of PDA, CNF, and CNF<sub>p</sub>, (b) TEM images and (c) TEM mapping of CNF<sub>p</sub>, (d) XRD patterns, (e) FT-IR plots, and (f) TGA-DTG curves of CN, CN/CNF, and CN/CNF<sub>p</sub>, SEM images of (g) CN, (h) CN/CNF, and (i) CN/CNF<sub>p</sub>.

higher than those of most g-C<sub>3</sub>N<sub>4</sub>-based photocatalysts (Fig. 3i, Table S2).

### 3.3. Mechanism of photocatalytic H<sub>2</sub>O<sub>2</sub> production

Firstly, the band structures of three photocatalysts were explored. Fig. 4a displays the calculated band gap energy ( $E_g$ ) from UV-vis DRS spectra (Fig. S7) of different photocatalysts, which remains relatively unchanged (CN: 2.83 eV, CN/CNF: 2.80 eV, and CN/CNF<sub>p</sub>: 2.91 eV) [48]. The XPS valence band ( $E_{VB-XPS}$ ) potentials of the three samples were further obtained through XPS analysis (Fig. S8a), and the flat band ( $E_{fb}$ ) potentials were determined by Mott-Schottky plots (Fig. S9). Therefore, the corrected valence band ( $E_{VB}$ ) potentials of CN (+1.59 eV), CN/CNF (+1.60 eV), and CN/CNF<sub>p</sub> (+1.59 eV) were calculated via the equation ( $E_{VB} = E_{VB-XPS} + E_{fb} + E_{Ag/AgCl}^0$ , where  $E_{Ag/AgCl}^0 = 0.2$  eV) [35]. Furthermore, the conduction band ( $E_{CB}$ ) potentials of CN (-1.26 eV), CN/CNF (-1.20 eV), and CN/CNF<sub>p</sub> (-1.32 eV) were calculated by the formula ( $E_{CB} = E_{VB} - E_g$ ) [49]. Fig. S8b shows the energy band structures of CN, CN/CNF, and CN/CNF<sub>p</sub>, and it can be observed that there is not a significant variation in three photocatalysts.

To examine the chemical composition of the different photocatalysts, X-ray photoelectron spectroscopy (XPS) analysis was performed. As shown in Fig. S10a, all three samples exhibit the presence of C and N elements. In addition, CN/CNF and CN/CNF<sub>p</sub> samples also show the

presence of O elements, indicating the successful incorporation of CNF and CNF<sub>p</sub> onto the surface of CN. Based on the high-resolution C1s-XPS spectra (Fig. 4b), CN/CNF and CN/CNF<sub>p</sub> exhibit three peaks around 284.8 eV, 286.6 eV, and 288.2 eV, attributed to C-C, C-O, and N=C-N, respectively [50]. However, pure CN only has two peaks at 284.8 eV and 288.2 eV [51,52], which is consistent with the absence of O element shown in XPS survey (Fig. S10a). Additionally, the N=C-N peak of three samples shifts to lower binding energy successively. The N1s-XPS spectra (Fig. 4c) illustrates that the peak of 398.9 eV, 400.4 eV, and 401.5 eV correspond to the C=N-C, N-C<sub>3</sub>, and C-NH<sub>x</sub>, respectively [53]. Specifically speaking, there is a decrease of C-NH<sub>x</sub> following the order of CN (9.6%) > CN/CNF (8.8%) > CN/CNF<sub>p</sub> (4.6%), demonstrating that the introduction of CNF and CNF<sub>p</sub> may consume the edge amino groups (-NH<sub>2</sub>) of pure CN. Moreover, analogous to the shift of N-C=N (Fig. 4b), the entire N1s-XPS peaks of three photocatalysts show the same shift to lower binding energy, which further confirms the enhancing effect of CNF and CNF<sub>p</sub> on the electron cloud density of C and N in pure CN [25, 28]. Fig. S10b presents the O1s-XPS spectra, where the peak of 530.5, 532.5 and 533.2 eV for CN/CNF and CN/CNF<sub>p</sub> (except pure CN) originates from C=O, absorbed H<sub>2</sub>O [54] and O<sub>2</sub> [55], possibly attributed to the introduction of CNF and CNF<sub>p</sub>. This result can be further confirmed by the temperature programmed desorption (TPD) in O<sub>2</sub> that CN/CNF<sub>p</sub> (1171.85) exhibits the best capacity for O<sub>2</sub> absorption than CN/CNF (981.51) and CN (829.42), as depicted in Fig. S11 [56].



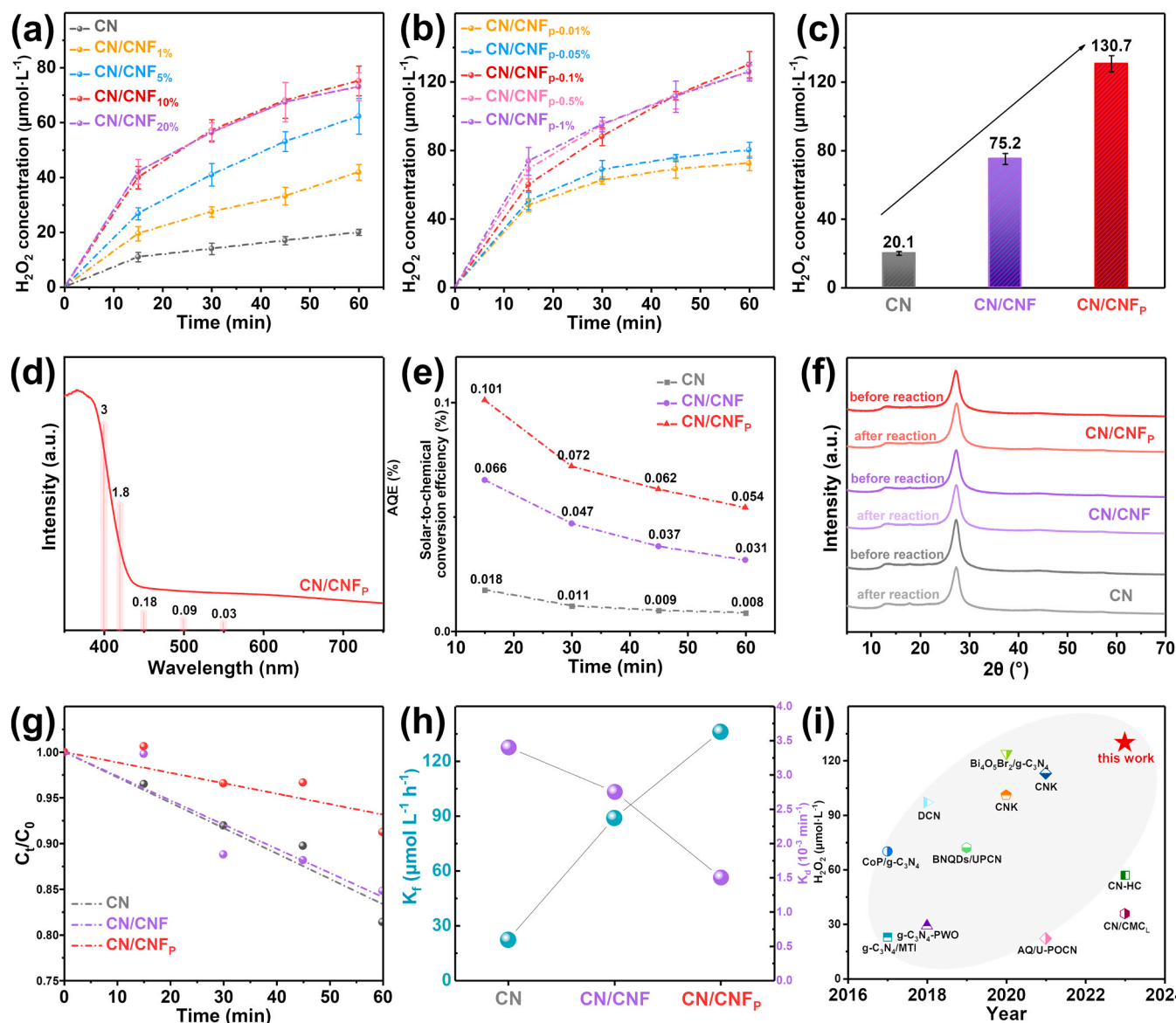


**Fig. 3.** (a) PHP for CN and CN/CNF (1%, 5%, 10%, and 20%), (b) PHP for CN/CNF<sub>p</sub> (0.01%, 0.05%, 0.1%, 0.5%, and 1%), (c) the PHP for CN, CN/CNF, and CN/CNF<sub>p</sub>, (d) wavelength-dependent apparent quantum efficiency (AQE) of CN/CNF<sub>p</sub>, (e) solar-to-chemical conversion efficiency (SCC), (f) XRD patterns before and after photocatalytic reaction, (g) photocatalytic H<sub>2</sub>O<sub>2</sub> decomposition and (h) plot of photocatalytic H<sub>2</sub>O<sub>2</sub> formation rate (K<sub>f</sub>) and photocatalytic H<sub>2</sub>O<sub>2</sub> decomposition rate (K<sub>d</sub>) of photocatalysts, (i) PHP comparison of g-C<sub>3</sub>N<sub>4</sub>-based photocatalysts in recent years (reaction time: 1 h).

Zeta potential measurements were conducted to observe the surface charge of different photocatalysts. As presented in Fig. 4d, the increasing order of absolute Zeta potential values are as follows: CN (15.6 mV) < CN/CNF (25.2 mV) < CN/CNF<sub>p</sub> (27.6 mV), indicating that the negative hydroxyl/carboxyl groups (-OH/COOH) of CNF and the negative benzene ring of PDA have altered the surface charge distribution of pristine CN [57]. Based on this result, it can be inferred that hydrogen bonding and  $\pi$ - $\pi$  stacking are possibly formed between CN and CNF<sub>p</sub>. To validate this hypothesis, the molecular electrostatic potential (MESP) analysis of three samples, based on density functional theory (DFT), was conducted. Fig. 4e exhibits that the presence of a red-blue interface region provides evidence for the occurrence of hydrogen bonding between CN and CNF<sub>p</sub> [58]. In addition, the reduced density gradient (RDG) further confirms the hydrogen bonding between CN and CNF (Fig. 4f), as well as the  $\pi$ - $\pi$  stacking between CN and PDA (Fig. S12) [59]. Besides, in contrast to CN/CNF, Fig. 4g illustrates the simultaneous occurrence of hydrogen bonding and stronger  $\pi$ - $\pi$  stacking (sign ( $\lambda_2$ )  $\rho$  = -0.02 to 0: a larger spike) in CN/CNF<sub>p</sub>.

To investigate the influence of hydrogen bonding/ $\pi$ - $\pi$  stacking on photocatalytic activity, the photoluminescence (PL), time-resolved photoluminescence (TRPL), transient photocurrent response (TPR), and electrochemical impedance spectra (EIS) of the three samples were applied to analyze the charge separation and migration capabilities in PHP. As illustrated in Fig. 5a, the PL intensity of CN, CN/CNF, and CN/CNF<sub>p</sub> gradually levels off, indicating that CN/CNF<sub>p</sub> exhibits the highest capability for photogenerated electron-hole pair separation [60]. Moreover, the lifetimes of photogenerated charge carriers (Fig. S13) in the photocatalysts are as follows: CN (8.66 ns) > CN/CNF (7.12 ns) > CN/CNF<sub>p</sub> (5.37 ns), which may be attributed to improved photoexcitation dissociation in CN/CNF and CN/CNF<sub>p</sub> [61]. At the same time, Fig. 5b displays the transient photocurrent values of CN, CN/CNF, and CN/CNF<sub>p</sub>, which are 0.085, 0.06, and 0.03  $\mu$ A·cm<sup>-2</sup>, respectively, indicating that the introduction of CNF<sub>p</sub> significantly promotes the migration of photogenerated charge carriers in CN [62]. Additionally, the Nyquist plots (Fig. 5c) of the three samples confirm that CN/CNF<sub>p</sub> exhibits the highest efficiency in photogenerated charge carrier

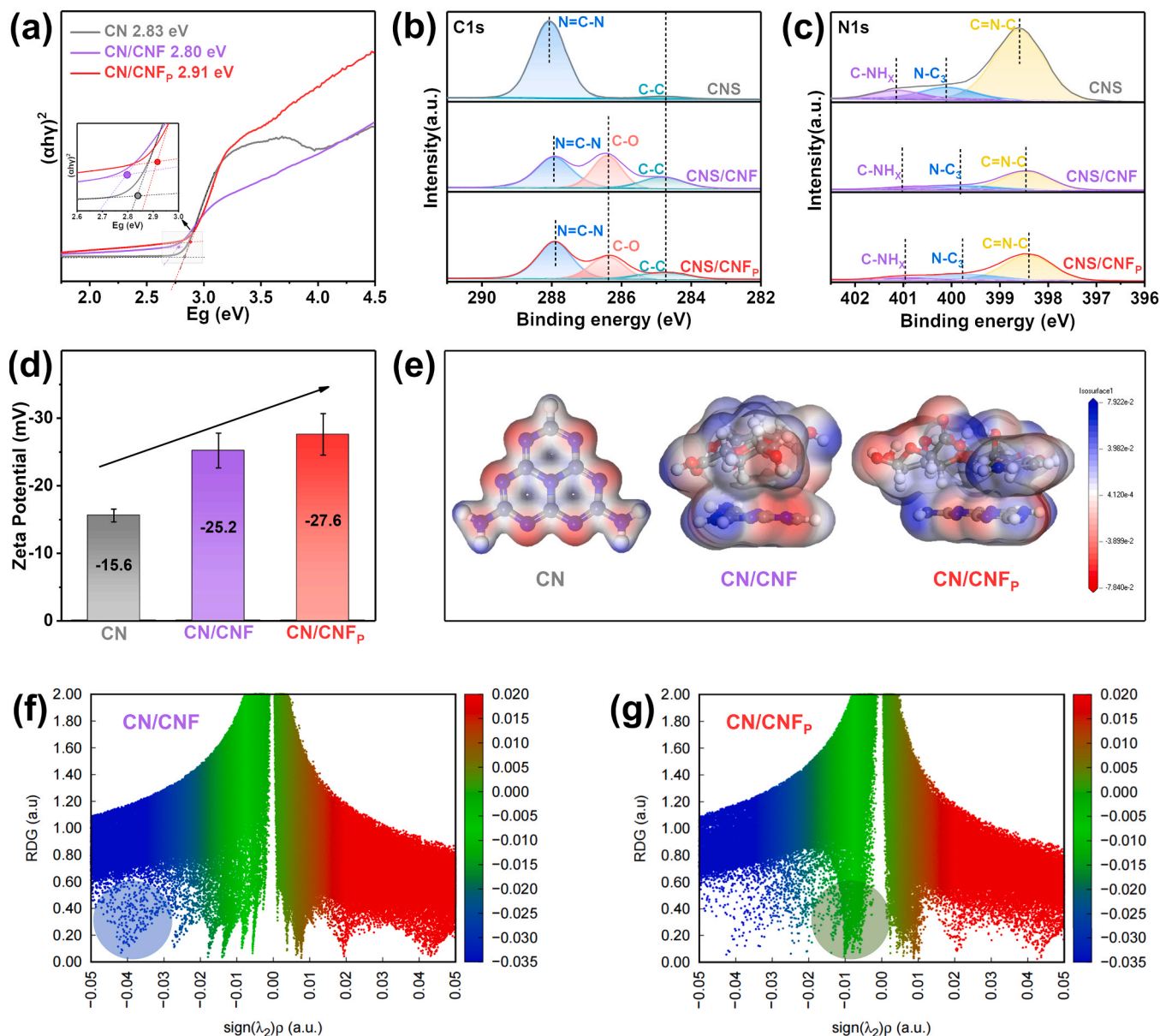


**Fig. 4.** (a) Calculated energy band gap, (b) C1s XPS spectra, (c) N1s XPS spectra, (d) Zeta potential, and (e) electrostatic potential of CN, CN/CNF, and CN/CNF<sub>p</sub>: red area, white area, and blue area represent positive charge, neutral charge, and negative charge, respectively, and reduced density gradient (RDG) of (f) CN/CNF and (g) CN/CNF<sub>p</sub>: blue, green and red refer to H-bond, van der Waals and steric resistance in ring, respectively.

migration, as evidenced by the arc radius values ( $R_{CN} > R_{CN/CNF} > R_{CN/CNF_p}$ ) [63]. To further investigate the promotion mechanism of CNF<sub>p</sub> on the PHP of CN, the different charge density and HOMO-LUMO analysis were performed by DFT calculation. As shown in Fig. 5d, CNF<sub>p</sub> further promotes the transfer of electron, which can be seen that rich-electron area is more concentrated on CN in CN/CNF<sub>p</sub> in contrast to CN/CNF [64,65]. This also be confirmed by the HOMO-LUMO analysis (Fig. 5e) of CN/CNF<sub>p</sub> [66]. In summary, compared to CNF, CNF<sub>p</sub> further facilitates the separation and migration of photo-generated charges in CN/CNF<sub>p</sub>.

The pathway of PHP in the three samples were investigated first using the scavenger method with 1 mM EDTA-2Na ( $h^+$ ), 0.5 mM AgNO<sub>3</sub> ( $e^-$ ), and 1 mM p-benzoquinone (PBQ,  $\cdot O_2^-$ ). As depicted in Fig. 5f, after the addition of EDTA-2Na, there is an increase in PHP of all photocatalysts, indicating that the water oxidation reaction (WOR) pathway (Eq. 1) is not the main part of PHP [67]. Based on this result, it is hypothesized that the oxygen reduction reaction (ORR) is the main pathway of PHP. The speculation is further supported by the significant

decrease of PHP when adding AgNO<sub>3</sub> or PBQ scavenger. The significant performance degradation observed after the addition of AgNO<sub>3</sub> suggests that all three photocatalysts primarily rely on ORR pathway [68]. Furthermore, the substantial decrease in performance of PHP after the addition of PBQ indicates that three samples predominantly undergo a two-step single-electron ORR (Eq. 2 and Eq. 3), involving the  $\cdot O_2^-$  intermediate, instead of a one-step single-electron ORR (Eq. 4) [69]. In comparison to CN, the CN/CNF<sub>p</sub> sample exhibits the strongest electromagnetic paramagnetic resonance (EPR) signal (Fig. 5g), indicating a significantly higher  $\cdot O_2^-$  content generated during the photocatalytic process compared to CN, which aligns with the speculation that three photocatalysts mainly exhibits a two-step single-electron ORR [70].



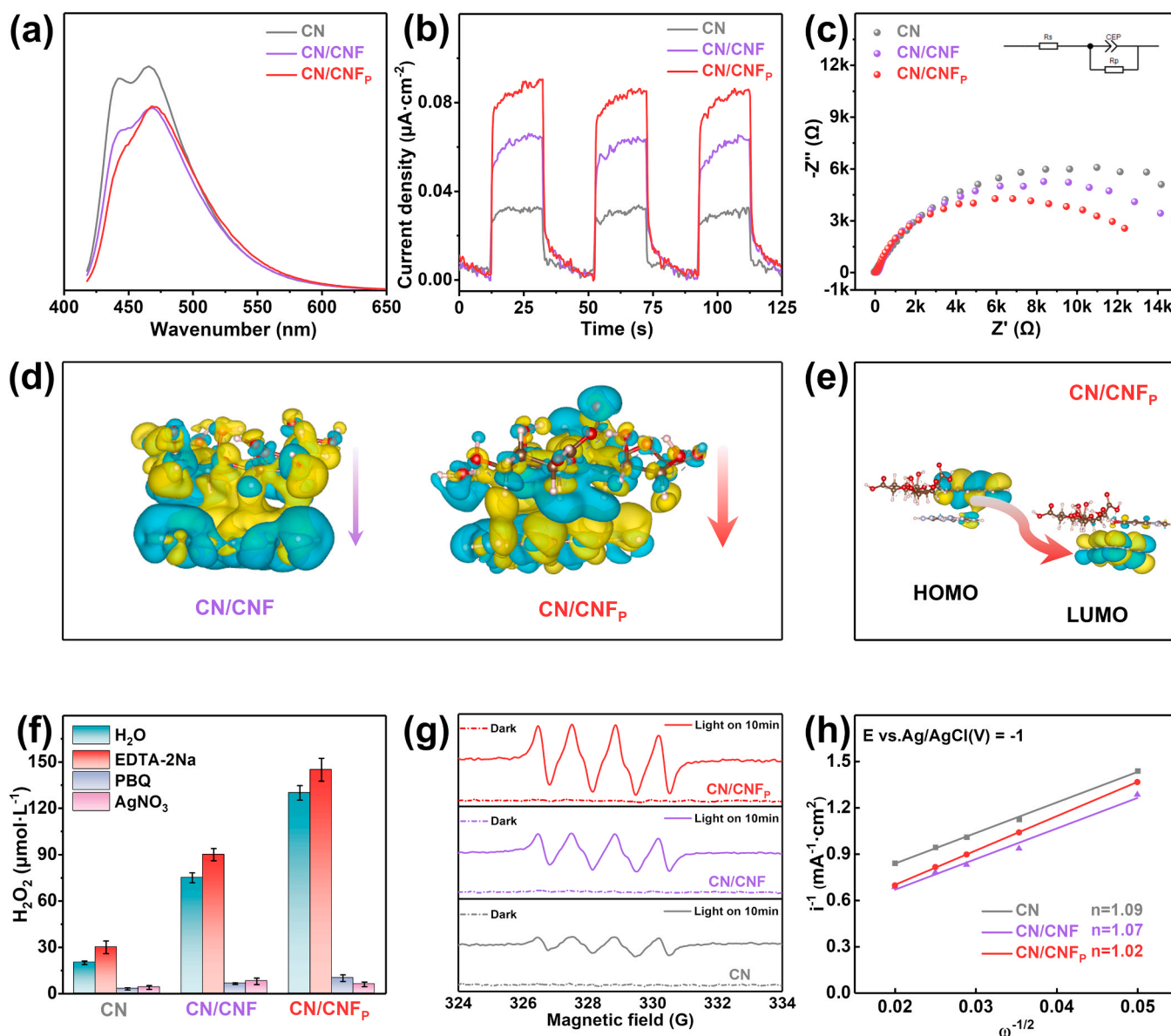


**Fig. 5.** (a) Photoluminescence (PL) spectra, (b) transient photocurrent response (TPR) curves, and (c) electrochemical impedance spectra (EIS) of CN, CN/CNF, and CN/CNF<sub>p</sub>, (d) different charge density of CN/CNF and CN/CNF<sub>p</sub> (blue: non-electron area, yellow: rich-electron area), (e) HOMO-LUMO plot of CN/CNF<sub>p</sub>, (f) comparative PHP (reaction time: 1 h, before and after the addition of EDTA-2Na (1 mM), p-benzoquinone (1 mM), and AgNO<sub>3</sub> (0.5 mM)), (g) electromagnetic paramagnetic resonance (EPR) spectra of 5,5-dimethyl-1-pyrroline N-oxide (DMPO)-O<sub>2</sub><sup>•-</sup>, and (h) Koutecky-Levich plots of CN, CN/CNF, and CN/CNF<sub>p</sub>.



Moreover, the Koutecky-Levich plots (Fig. 5h, Fig. S14) calculated via Eq. 5 and Eq. 6 demonstrate the average electron transfer numbers ( $n$ ): CN (1.09), CN/CNF (1.07), and CN/CNF<sub>p</sub> (1.02), indicating that CN/CNF<sub>p</sub> is more inclined to a two-step single-electron ORR in contrast to CN [71].

$$j^{-1} = j_k^{-1} + B^{-1} \omega^{-1/2} \quad (5)$$

$$B = 0.2nFv^{-1/2}CD^{2/3} \quad (6)$$

In the equation,  $j$  represents the measured current density,  $j_k$  denotes the kinetic current density,  $\omega$  corresponds to the rotational speed (rpm),  $F$  signifies the Faraday constant (96485 C·mol<sup>-1</sup>),  $v$  is the kinetic viscosity of water (0.01 cm<sup>2</sup>·s<sup>-1</sup>),  $C$  indicates the bulk concentration of O<sub>2</sub> in water (1.26 × 10<sup>-3</sup> mol·cm<sup>-3</sup>), and  $D$  symbolizes the diffusion coefficient of O<sub>2</sub> (2.7 × 10<sup>-5</sup> cm<sup>2</sup>·s<sup>-1</sup>).

To further study the precise mechanism of photocatalysis, in-situ Fourier transform infrared (in-situ FT-IR) spectroscopy was performed. Fig. 6a-f shows the FT-IR spectra of PHP by CN, CN/CNF, and CN/CNF<sub>p</sub> in pure water solution continuously bubbled with O<sub>2</sub>. All characteristic peaks between 1000 and 1500 cm<sup>-1</sup> gradually intensify as the time extends with an interval of two minutes. The bands at 1156, 1278 and 1362 cm<sup>-1</sup> were corresponded to the ·O<sub>2</sub><sup>•-</sup>, O-O stretching mode of surface-adsorbed superoxide \*OOH and the OOH bending mode of \*HOOH, respectively. This indicates the formation of H<sub>2</sub>O<sub>2</sub> on the surfaces of the three photocatalysts through a superoxide intermediate pathway. Moreover, the spectral bands at 1103 and 1434 cm<sup>-1</sup> were attributed to C-OH and C=O, respectively, indicating the presence of OH\* as an important intermediate species during the PHP [62]. All these findings confirm the formation of ·O<sub>2</sub><sup>•-</sup> and \*OOH intermediates and the two-step single-electron ORR pathway.

In summary, Fig. 6g illustrates the mechanism of PHP by CN/CNF<sub>p</sub> photocatalyst, which is obtained by combining CN and CNF<sub>p</sub> via



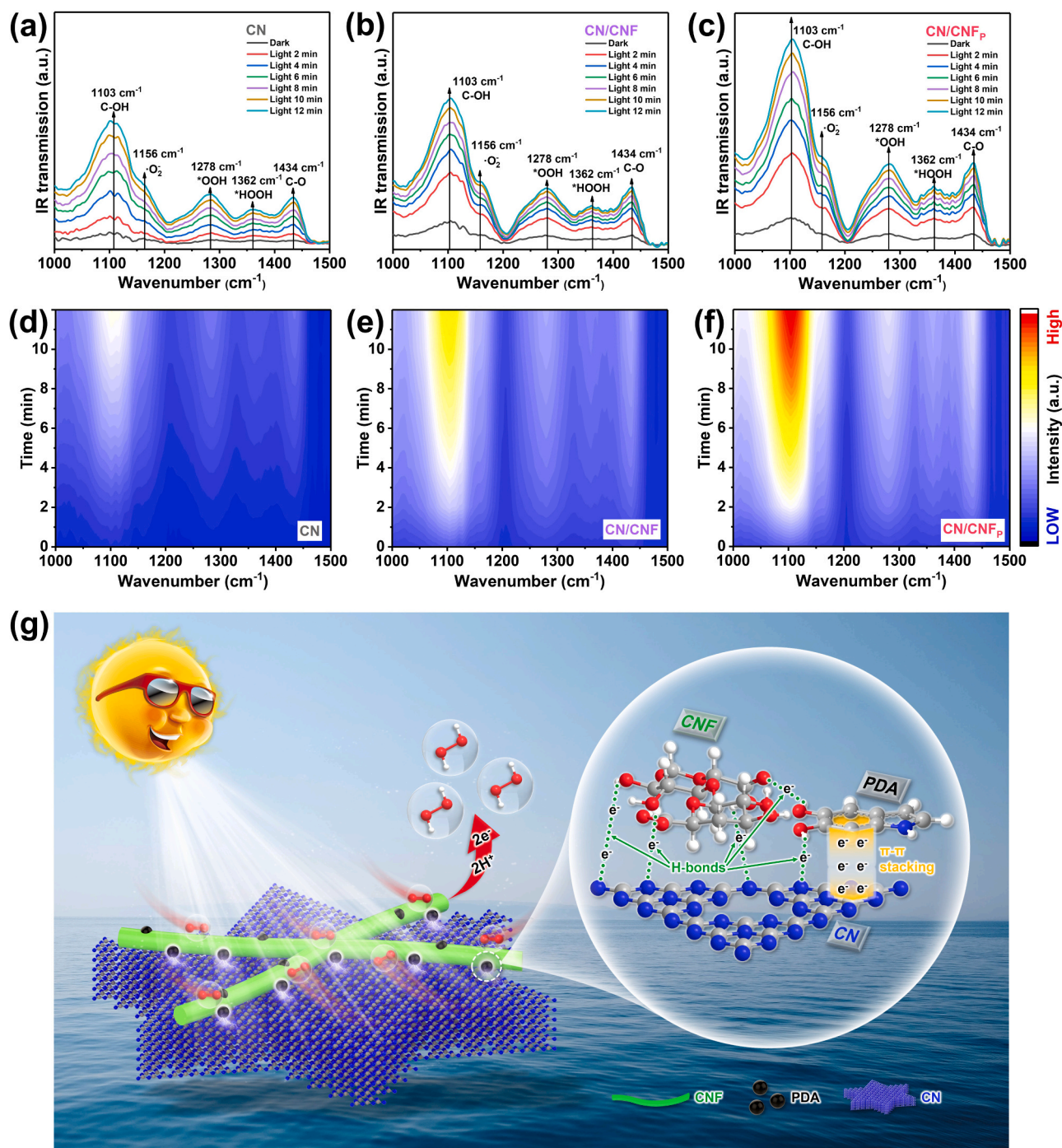


**Fig. 6.** In-situ FT-IR spectra of (a) (d) CN, (b) (e) CN/CNF, and (c) (f) CN/CNF<sub>p</sub> at 1000~1500 cm<sup>-1</sup> during the PHP in pure water bubbled with O<sub>2</sub>, and (g) possible mechanism of PHP for CN/CNF<sub>p</sub>.

hydrogen bonding and  $\pi$ - $\pi$  stacking. Experimental tests have revealed that CN/CNF<sub>p</sub> exhibits outstanding PHP performance (130.7  $\mu\text{mol}\cdot\text{L}^{-1}\cdot\text{h}^{-1}$ ) under visible light irradiation in a pure water system, which is approximately 6.5 times superior to that of pure CN (20.1  $\mu\text{mol}\cdot\text{L}^{-1}\cdot\text{h}^{-1}$ ). DFT confirmed that the enhancement can be attributed to the further promotion of electron transfer and separation. Through the enhanced two-step single-electron ORR pathway, a significant amount of  $\cdot\text{O}_2^-$  is generated, which leads to superior PHP performance.

#### 4. Conclusions

In summary, biomimetic Polydopamine (PDA) and carboxylated

cellulose nanofibers (CNF) decorated carbon nitride (g-C<sub>3</sub>N<sub>4</sub>, CN) bridged with multiple hydrogen bonds and  $\pi$ - $\pi$  stacking were successfully fabricated by a simple and mild method. Using PDA and CNF as green electron mediators, CN/CNF<sub>p</sub> (130.7  $\mu\text{mol}\cdot\text{L}^{-1}\cdot\text{h}^{-1}$ ) exhibits superior PHP performance with enhancements of 1.7-fold and 6.5-fold compared to CN/CNF (75.2  $\mu\text{mol}\cdot\text{L}^{-1}\cdot\text{h}^{-1}$ ) and CN (20.1  $\mu\text{mol}\cdot\text{L}^{-1}\cdot\text{h}^{-1}$ ), respectively. Experimental and DFT calculations have validated that the introduction of CNF<sub>p</sub> exhibits multiple effects attributed to the hydrogen bonding/ $\pi$ - $\pi$  stacking between CN and CNF<sub>p</sub>, including: (1) facilitated O<sub>2</sub> adsorption, (2) accelerated separation and transfer of photogenerated charge carriers, and (3) favorable selective 2e<sup>-</sup> ORR. Our work offers a rational design concept for highly efficient

photocatalysts for H<sub>2</sub>O<sub>2</sub> production. Moreover, the novel insight of interfacial multiple hydrogen bonds and  $\pi$ - $\pi$  bonds as high-speed charge transfer channels provides new opportunities for designing advanced photocatalysts.

### CRediT authorship contribution statement

**Lihui Chen:** Supervision, Resources, Investigation, Funding acquisition. **Jingde Li:** Writing – review & editing, Supervision, Software, Investigation. **Liulian Huang:** Resources, Funding acquisition. **Yu Wang:** Investigation, Formal analysis. **Tianshang Shan:** Writing – original draft, Software, Formal analysis, Data curation. **He Xiao:** Writing – review & editing, Supervision, Resources, Investigation, Funding acquisition. **Fengshan Zhang:** Resources, Funding acquisition. **Hui Wu:** Supervision, Resources. **Zhichun Huang:** Investigation, Formal analysis. **Dan Luo:** Formal analysis.

### Declaration of Competing Interest

The authors declare that they have no known competing financial interests or personal relationships that could have appeared to influence the work reported in this paper.

### Data Availability

No data was used for the research described in the article.

### Acknowledgments

This work was supported by the Natural Science Foundation of Fujian (2022J01144), Natural Science Foundation of Shandong (ZR2021MC035), and Innovation and Entrepreneurship Training Program for College Students (X202310389326). Technical support given by Shuaichong Wei, Boxuan Jin, and Shengnan Tian of Hebei University of Technology are also acknowledged.

### Appendix A. Supporting information

Supplementary data associated with this article can be found in the online version at [doi:10.1016/j.apcatb.2024.123872](https://doi.org/10.1016/j.apcatb.2024.123872).

### References

- [1] J.K. Edwards, B. Solsona, E.N. N, A.F. Carley, A.A. Herzog, C.J. Kiely, G. J. Hutchings, Switching off hydrogen peroxide hydrogenation in the direct synthesis process, *Science* 323 (2009) 1037–1041.
- [2] J.-P. Shang, P. Liang, Y. Peng, D.-F. Xu, Y.-B. Li, One-step treatment for upgrading bleached bamboo pulp to dissolving pulp high solvency in green alkali/urea aqueous solution, *Polymers* (2023).
- [3] S. He, C. Xie, Y. Jiang, K. Pu, An organic afterglow protheranostic nanoassembly, *Adv. Mater.* 31 (2019) 1902672.
- [4] Y. Lee, D.L. Sedlak, U. von Gunten, Oxidative water treatment: the track ahead, *Environ. Sci. Technol.* 57 (2023) 18391–18392.
- [5] J.M. Campos-Martin, G. Blanco-Brieva, J.L.G. Fierro, Hydrogen peroxide synthesis: an outlook beyond the anthraquinone process, *Angew. Chem. Int. Ed.* 45 (2006) 6962–6984.
- [6] S. Yan, Y. Li, X. Yang, X. Jia, J. Xu, H. Song, Photocatalytic H<sub>2</sub>O<sub>2</sub> generation reaction with a benchmark rate at air-liquid-solid joint interfaces, *Adv. Mater.* (2023) 2307967.
- [7] S. Siahrostami, A. Verdager-Casadevall, M. Karamad, D. Deiana, P. Malacrida, B. Wickman, M. Escudero-Escribano, E.A. Paoli, R. Frydendal, T.W. Hansen, I. Chorkendorff, I.E.L. Stephens, J. Rossmeisl, Enabling direct H<sub>2</sub>O<sub>2</sub> production through rational electrocatalyst design, *Nat. Mater.* 12 (2013) 1137–1143.
- [8] H.-c. Li, Q. Wan, C. Du, J. Zhao, F. Li, Y. Zhang, Y. Zheng, M. Chen, K.H.L. Zhang, J. Huang, G. Fu, S. Lin, X. Huang, H. Xiong, Layered Pd oxide on PdSn nanowires for boosting direct H<sub>2</sub>O<sub>2</sub> synthesis, *Nat. Commun.* 13 (2022) 6072.
- [9] P. Kumar, G. Singh, X. Guan, J. Lee, R. Bahadur, K. Ramadass, P. Kumar, M. G. Kibria, D. Vidyasagar, J. Yi, A. Vinu, Multifunctional carbon nitride nanoarchitectures for catalysis, *Chem. Soc. Rev.* 52 (2023) 7602–7664.
- [10] Q. Wang, X.Y. Kong, Y. Wang, L. Wang, Y. Huang, H. Li, T. Ma, L. Ye, Metal-Free photocatalysts for conversion of H<sub>2</sub>O into hydrogen peroxide, *ChemSusChem* 15 (2022) e202201514.
- [11] Y. Xia, B. Zhu, X. Qin, W. Ho, J. Yu, Zinc porphyrin/g-C<sub>3</sub>N<sub>4</sub> S-scheme photocatalyst for efficient H<sub>2</sub>O<sub>2</sub> production, *Chem. Eng. J.* 467 (2023) 143528.
- [12] Z. Wei, M. Liu, Z. Zhang, W. Yao, H. Tan, Y. Zhu, Efficient visible-light-driven selective oxygen reduction to hydrogen peroxide by oxygen-enriched graphitic carbon nitride polymers, *Energy Environ. Sci.* 11 (2018) 2581–2589.
- [13] Y. Zhang, Q. Cao, A. Meng, X. Wu, Y. Xiao, C. Su, Q. Zhang, Molecular heptazine-triazine junction over carbon nitride frameworks for artificial photosynthesis of hydrogen peroxide, *Adv. Mater.* 35 (2023) 2306831.
- [14] Q. Chen, C. Lu, B. Ping, G. Li, J. Chen, Z. Sun, Y. Zhang, Q. Ruan, L. Tao, A hydroxyl-induced carbon nitride homojunction with functional surface for efficient photocatalytic production of H<sub>2</sub>O<sub>2</sub>, *Appl. Catal. B: Environ.* 324 (2023) 122216.
- [15] Y. Zhao, Y. Liu, Z. Wang, Y. Ma, Y. Zhou, X. Shi, Q. Wu, X. Wang, M. Shao, H. Huang, Y. Liu, Z. Kang, Carbon nitride assisted 2D conductive metal-organic frameworks composite photocatalyst for efficient visible light-driven H<sub>2</sub>O<sub>2</sub> production, *Appl. Catal. B: Environ.* 289 (2021) 120035.
- [16] W. Ling, J. Ma, Z. Liu, R. Cui, J. Zhang, X. Li, M. Hong, R. Sun, Enhancing biomass oxidation with carbon nitride nanosheets ring inserted on C. I. Pigment Yellow 53 photocatalysts for simultaneous CO and lactic acid production, *Chem. Eng. J.* 475 (2023) 146117.
- [17] J. Xiong, X. Li, J. Huang, X. Gao, Z. Chen, J. Liu, H. Li, B. Kang, W. Yao, Y. Zhu, CN/rGO@BPQDs high-low junctions with stretching spatial charge separation ability for photocatalytic degradation and H<sub>2</sub>O<sub>2</sub> production, *Appl. Catal. B: Environ.* 266 (2020) 118602.
- [18] Z. Liu, J. Ma, Y. Guo, M. Hong, R. Sun, Photocatalytic CO<sub>2</sub> reduction integrated with biomass selective oxidation via single-atom Ru and P dual sites on carbon nitride, *Appl. Catal. B: Environ.* 342 (2024) 123429.
- [19] Z. Liu, J. Ma, M. Hong, R. Sun, Potassium and sulfur dual sites on highly crystalline carbon nitride for photocatalytic biorefinery and CO<sub>2</sub> reduction, *ACS, Catalysis* 13 (2023) 2106–2117.
- [20] C. Tian, X. Tao, S. Luo, Y. Qing, X. Lu, J. She, Y. Wu, Cellulose nanofibrils anchored Ag on graphitic carbon nitride for efficient photocatalysis under visible light, *Environ. Sci.: Nano* 5 (2018) 2129–2143.
- [21] Y. Xu, W. Li, T. Xu, G. Wang, W. Huan, C. Si, Straightforward fabrication of lignin-derived carbon-bridged graphitic carbon nitride for improved visible photocatalysis of tetracycline hydrochloride assisted by peroxymonosulfate activation, *Adv. Compos. Hybrid. Mater.* 6 (2023) 197.
- [22] Y. Zheng, Y. Luo, Q. Ruan, S. Wang, J. Yu, X. Guo, W. Zhang, H. Xie, Z. Zhang, Y. Huang, Plasma-induced hierarchical amorphous carbon nitride nanostructure with two N<sub>2</sub> C-site vacancies for photocatalytic H<sub>2</sub>O<sub>2</sub> production, *Appl. Catal. B: Environ.* 311 (2022) 121372.
- [23] Q. He, J. Ding, H.-J. Tsai, Y. Liu, M. Wei, Q. Zhang, Z. Wei, Z. Chen, J. Huang, S.-F. Hung, H. Yang, Y. Zhai, Boosting photocatalytic hydrogen peroxide production by regulating electronic configuration of single Sb atoms via carbon vacancies in carbon nitrides, *J. Colloid Interface Sci.* 651 (2023) 18–26.
- [24] R. Zou, Z. Chen, L. Zhong, W. Yang, T. Li, J. Gan, Y. Yang, Z. Chen, H. Lai, X. Li, C. Liu, S. Admassie, E.I. Iwuoha, J. Lu, X. Peng, Nanocellulose-assisted molecularly engineering of nitrogen deficient graphitic carbon nitride for selective biomass photo-oxidation, *Adv. Funct. Mater.* 33 (2023) 2301311.
- [25] P. Zhang, J. Zhang, D. Wang, F. Zhang, Y. Zhao, M. Yan, C. Zheng, Q. Wang, M. Long, C. Chen, Modification of g-C<sub>3</sub>N<sub>4</sub> with hydroxyethyl cellulose as solid proton donor via hydrogen bond to enhance H<sub>2</sub>O<sub>2</sub> production, *Appl. Catal. B: Environ.* 318 (2022) 121749.
- [26] C. Xue, P. Wang, H. Che, W. Liu, B. Liu, Y. Ao, Simultaneous organic pollutant degradation and hydrogen peroxide production by molecular-engineered carbon nitride, *Appl. Catal. B: Environ.* 340 (2024) 123259.
- [27] X. Zeng, Y. Liu, Y. Kang, Q. Li, Y. Xia, Y. Zhu, H. Hou, M.H. Uddin, T. R. Gengenbach, D. Xia, C. Sun, D.T. McCarthy, A. Deletic, J. Yu, X. Zhang, Simultaneously tuning charge separation and oxygen reduction pathway on graphitic carbon nitride by polyethylenimine for boosted photocatalytic hydrogen peroxide production, *ACS Catal.* 10 (2020) 3697–3706.
- [28] T. Shan, J. Li, S. Wu, H. Wu, F. Zhang, G. Liao, H. Xiao, L. Huang, L. Chen, Boosting H<sub>2</sub>O<sub>2</sub> production over carboxymethyl cellulose modified g-C<sub>3</sub>N<sub>4</sub> via hydrogen-bonding-assisted charge transfer, *Chem. Eng. J.* 478 (2023) 147509.
- [29] S. Sankhla, S. Mondal, S. Neogi, Pyrolysis of cellulose nanofibers: detailed assessment of process kinetics and thermodynamic parameters, *Cellulose* 30 (2023) 7695–7712.
- [30] D. Stanisic, G.C.F. Cruz, L.A. Elias, J. Tsukamoto, C.W. Arns, D. Soares da Silva, S. Mochkalev, R. Savu, L. Tasic, High-resolution magic-angle spinning NMR spectroscopy for evaluation of cell shielding by virucidal composites based on biogenic silver nanoparticles, flexible cellulose nanofibers and graphene oxide, *Front. Bioeng. Biotechnol.* 10 (2022).
- [31] U. Edlund, T. Lagerberg, E. Ålander, Admicellar Polymerization Coating of CNF Enhances Integration in Degradable Nanocomposites, *Biomacromolecules* 20 (2019) 684–692.
- [32] Z. Li, J. Guan, C. Yan, N. Chen, C. Wang, T. Liu, F. Cheng, Q. Guo, X. Zhang, X. Ye, Y. Liu, Z. Shao, Corn straw core/cellulose nanofibers composite for food packaging: Improved mechanical, bacteria blocking, ultraviolet and water vapor barrier properties, *Food Hydrocoll.* 143 (2023) 108884.
- [33] Y. Liu, K. Ai, L. Lu, Polydopamine and its derivative materials: synthesis and promising applications in energy, environmental, and biomedical fields, *Chem. Rev.* 114 (2014) 5057–5115.
- [34] H. Hemmatpour, O. De Luca, D. Crestani, M.C.A. Stuart, A. Lasorsa, P.C.A. van der Wel, K. Loos, T. Giousis, V. Haddadi-Asl, P. Rudolf, New insights in polydopamine formation via surface adsorption, *Nat. Commun.* 14 (2023) 664.

- [35] H. Luo, T. Shan, J. Zhou, L. Huang, L. Chen, R. Sa, Y. Yamauchi, J. You, Y. Asakura, Z. Yuan, H. Xiao, Controlled synthesis of hollow carbon ring incorporated g-C<sub>3</sub>N<sub>4</sub> tubes for boosting photocatalytic H<sub>2</sub>O<sub>2</sub> production, *Appl. Catal. B: Environ.* 337 (2023) 122933.
- [36] J. Zhou, T. Shan, H. Luo, B. Boury, X. Xu, H. Wu, F. Zhang, H. Xiao, Enhanced single-electron transfer for efficiently photocatalytic H<sub>2</sub>O<sub>2</sub> production over g-C<sub>3</sub>N<sub>4</sub> decorated with TEMPO-oxidized cellulosic carbon, *J. Environ. Chem. Eng.* 11 (2023) 109512.
- [37] Q. Han, C. Zhang, T. Guo, Y. Tian, W. Song, J. Lei, Q. Li, A. Wang, M. Zhang, S. Bai, X. Yan, Hydrogel nanoarchitectonics of a flexible and self-adhesive electrode for long-term wireless electroencephalogram recording and high-accuracy sustained attention evaluation, *Adv. Mater.* 35 (2023) 2209606.
- [38] Y.-j. Wu, X.-h. Wu, T.-x. Tu, P.-f. Zhang, J.-t. Li, Y. Zhou, L. Huang, S.-g. Sun, Controlled synthesis of FeN<sub>x</sub>-CoN<sub>x</sub> dual active sites interfaced with metallic Co nanoparticles as bifunctional oxygen electrocatalysts for rechargeable Zn-air batteries, *Appl. Catal. B: Environ.* 278 (2020) 119259.
- [39] X. Chen, Y. Li, Y. Wang, F. Tang, M. Mu, J. Tang, Green extraction of natural antibacterial cellulose-based nanofibers from pine cone, *Cellulose* 30 (2023) 6219–6232.
- [40] A. Di, C. Schiele, S.E. Hadi, L. Bergström, Thermally insulating and moisture-resilient foams based on upcycled aramid nanofibers and nanocellulose, *Adv. Mater.* 35 (2023) 2305195.
- [41] H. Yang, L. Bai, Y. Duan, H. Xie, X. Wang, R. Zhang, X. Ji, C. Si, Upcycling corn straw into nanocelluloses via enzyme-assisted homogenization: Application as building blocks for high-performance films, *J. Clean. Prod.* 390 (2023) 136215.
- [42] S.H. Hassan, T.S. Velayutham, Y.W. Chen, H.V. Lee, TEMPO-oxidized nanocellulose films derived from coconut residues: physicochemical, mechanical and electrical properties, *Int. J. Biol. Macromol.* 180 (2021) 392–402.
- [43] J. Yu, C. Chen, F. Shi, R. Li, F. Chen, J. Tang, K.C. Chan, Z.-L. Xu, A multifunctional MXene-porous polydopamine interface for stable and dendrite-free zinc metal batteries, *Energy Storage Mater.* 63 (2023) 102966.
- [44] Y. Hu, S. Zhang, Z. Zhang, H. Zhou, B. Li, Z. Sun, X. Hu, W. Yang, X. Li, Y. Wang, S. Liu, D. Wang, J. Lin, W. Chen, S. Wang, Enhancing photocatalytic-transfer semi-hydrogenation of alkynes over Pd/C<sub>3</sub>N<sub>4</sub> through dual regulation of nitrogen defects and the Mott–Schottky effect, *Adv. Mater.* 35 (2023) 2304130.
- [45] L. Wang, Y. Hong, E. Liu, X. Duan, X. Lin, J. Shi, A bottom-up acidification strategy engineered ultrathin g-C<sub>3</sub>N<sub>4</sub> nanosheets towards boosting photocatalytic hydrogen evolution, *Carbon* 163 (2020) 234–243.
- [46] L. Sun, Z. Zhang, J. Bian, F. Bai, H. Su, Z. Li, J. Xie, R. Xu, J. Sun, L. Bai, C. Chen, Y. Han, J. Tang, L. Jing, A. Z-Scheme, Heterojunctional photocatalyst engineered with spatially separated dual redox sites for selective CO<sub>2</sub> reduction with water: insight by in situ  $\mu$ s-transient absorption spectra, *Adv. Mater.* 35 (2023) 2300064.
- [47] Y. Xiong, Y. Chen, N. Yang, C. Jin, Q. Sun, WC<sub>1-x</sub>-Coupled 3D porous defective g-C<sub>3</sub>N<sub>4</sub> for efficient photocatalytic overall water splitting, *Sol. RRL* 3 (2019) 1800341.
- [48] H. Zhang, X. Bai, Protonated g-C<sub>3</sub>N<sub>4</sub> coated Co<sub>9</sub>S<sub>8</sub> heterojunction for photocatalytic H<sub>2</sub>O<sub>2</sub> production, *J. Colloid Interface Sci.* 627 (2022) 541–553.
- [49] P. Sha, L. Huang, J. Zhao, Z. Wu, Q. Wang, L. Li, D. Bu, S. Huang, Carbon nitrides with grafted dual-functional ligands as electron acceptors and active sites for ultra-stable photocatalytic H<sub>2</sub>O<sub>2</sub> production, *ACS Catalysis* 13 (2023) 10474–10486.
- [50] Z. Zhang, R. Ji, Q. Sun, J. He, D. Chen, N. Li, H. Li, A. Marcomini, Q. Xu, J. Lu, Enhanced photocatalytic degradation of 2-chlorophenol over Z-scheme heterojunction of CdS-decorated oxygen-doped g-C<sub>3</sub>N<sub>4</sub> under visible-light, *Appl. Catal. B: Environ.* 324 (2023) 122276.
- [51] A. Wang, H. Liang, F. Chen, X. Tian, S. Yin, S. Jing, P. Tsiakaras, Facile synthesis of C<sub>3</sub>N<sub>4</sub>/NiIn<sub>2</sub>S<sub>4</sub> heterostructure with novel solar steam evaporation efficiency and photocatalytic H<sub>2</sub>O<sub>2</sub> production performance, *Appl. Catal. B: Environ.* 310 (2022) 121336.
- [52] X. Li, G. Fang, X. Qian, Q. Tian, Z-scheme heterojunction of low conduction band potential MnO<sub>2</sub> and biochar-based g-C<sub>3</sub>N<sub>4</sub> for efficient formaldehyde degradation, *Chem. Eng. J.* 428 (2022) 131052.
- [53] D. Li, C. Wen, J. Huang, J. Zhong, P. Chen, H. Liu, Z. Wang, Y. Liu, W. Lv, G. Liu, High-efficiency ultrathin porous phosphorus-doped graphitic carbon nitride nanosheet photocatalyst for energy production and environmental remediation, *Appl. Catal. B: Environ.* 307 (2022) 121099.
- [54] Q. You, C. Zhang, M. Cao, B. Wang, J. Huang, Y. Wang, S. Deng, G. Yu, Defects controlling, elements doping, and crystallinity improving triple-strategy modified carbon nitride for efficient photocatalytic diclofenac degradation and H<sub>2</sub>O<sub>2</sub> production, *Appl. Catal. B: Environ.* 321 (2023) 121941.
- [55] C. Liu, H. Dai, C. Tan, Q. Pan, F. Hu, X. Peng, Photo-Fenton degradation of tetracycline over Z-scheme Fe-g-C<sub>3</sub>N<sub>4</sub>/Bi<sub>2</sub>WO<sub>6</sub> heterojunctions: Mechanism insight, degradation pathways and DFT calculation, *Appl. Catal. B: Environ.* 310 (2022) 121326.
- [56] Y. Song, C. Zhou, Z. Zheng, P. Sun, Y. She, F. Huang, Z. Mo, J. Yuan, H. Li, H. Xu, Porous carbon nitride nanotubes efficiently promote two-electron O<sub>2</sub> reduction for photocatalytic H<sub>2</sub>O<sub>2</sub> production, *J. Alloy. Compd.* 934 (2023) 167901.
- [57] J. Wei, R. Zhao, D. Luo, X. Lu, W. Dong, Y. Huang, X. Cheng, Y. Ni, Atomically precise Ni<sub>6</sub>(SC<sub>2</sub>H<sub>4</sub>Ph)<sub>12</sub> nanoclusters on graphitic carbon nitride nanosheets for boosting photocatalytic hydrogen evolution, *J. Colloid Interface Sci.* 631 (2023) 212–221.
- [58] Y. Zhang, H. Zhu, B. Zhang, H. Yang, C.-H. Tan, C. Wang, J. Wen, L. Zong, Hydrogen bond-enhanced halogen bonding organocatalyst with C(sp<sup>3</sup>)-Br and sulfoxide moieties, *ACS Catal.* 13 (2023) 7103–7109.
- [59] R. Laplaza, F. Peccati, R. A. Boto, C. Quan, A. Carbone, J.-P. Piquemal, Y. Maday, J. Contreras-García, NCIPLOT and the analysis of noncovalent interactions using the reduced density gradient, *WIREs Comput. Mol. Sci.* 11 (2021) e1497.
- [60] J. Yue, H. Yang, S. Wang, C. Liu, L. Wang, Photocatalytic reaction induced by N<sup>δ-</sup> → W<sup>δ+</sup> in tungsten trioxide/carbon nitride for dual-path production of hydrogen peroxide towards ciprofloxacin degradation, *J. Colloid Interface Sci.* 653 (2024) 981–991.
- [61] P. Sun, Z. Chen, J. Zhang, G. Wu, Y. Song, Z. Miao, K. Zhong, L. Huang, Z. Mo, H. Xu, Simultaneously tuning electronic reaction pathway and photoactivity of P, O modified cyano-rich carbon nitride enhances the photosynthesis of H<sub>2</sub>O<sub>2</sub>, *Appl. Catal. B: Environ.* 342 (2024) 123337.
- [62] S. Li, B. Feng, X. Zhang, J. Tian, D. Wang, Y. Pei, M. Qiao, Y. Li, B. Zong, Multiple heteroatom-doped urea and thiourea-derived polymeric carbon nitride for high-performance visible light-driven photocatalytic O<sub>2</sub> reduction to H<sub>2</sub>O<sub>2</sub>, *Appl. Catal. B: Environ.* 335 (2023) 122879.
- [63] Z. Bao, Q. Cao, Y. Shao, S. Zhang, X. Peng, Y. Li, C. Jiang, X. Zhong, J. Wang, Carbon and oxygen-doped phosphorus nitride (COPN) for continuous selective and stable H<sub>2</sub>O<sub>2</sub> production, *ACS Catal.* 13 (2023) 14492–14502.
- [64] X. Zhang, B. Xu, S. Wang, X. Li, C. Wang, Y. Xu, R. Zhou, Y. Yu, H. Zheng, P. Yu, Y. Sun, Carbon nitride nanotubes anchored with high-density CuN<sub>x</sub> sites for efficient degradation of antibiotic contaminants under photo-Fenton process: performance and mechanism, *Appl. Catal. B: Environ.* 306 (2022) 121119.
- [65] X. Xiao, Z. Ruan, Q. Li, L. Zhang, H. Meng, Q. Zhang, H. Bao, B. Jiang, J. Zhou, C. Guo, X. Wang, H. Fu, A. Unique, Fe-N<sub>4</sub> coordination system enabling transformation of oxygen into superoxide for photocatalytic C-H activation with high efficiency and selectivity, *Adv. Mater.* 34 (2022) 2200612.
- [66] Z. Ma, X. Zong, Q. Hong, L. Niu, T. Yang, W. Jiang, D. Qu, L. An, X. Wang, Z. Kang, Z. Sun, Electrostatic potential of the incorporated asymmetry molecules induced high charge separation efficiency of the modified carbon nitride copolymers, *Appl. Catal. B: Environ.* 319 (2022) 121922.
- [67] Y. Yang, G. Zeng, D. Huang, C. Zhang, D. He, C. Zhou, W. Wang, W. Xiong, X. Li, B. Li, W. Dong, Y. Zhou, Molecular engineering of polymeric carbon nitride for highly efficient photocatalytic oxytetracycline degradation and H<sub>2</sub>O<sub>2</sub> production, *Appl. Catal. B: Environ.* 272 (2020) 118970.
- [68] L. Jian, Y. Dong, H. Zhao, C. Pan, G. Wang, Y. Zhu, Highly crystalline carbon nitrogen polymer with a strong built-in electric fields for ultra-high photocatalytic H<sub>2</sub>O<sub>2</sub> production, *Appl. Catal. B: Environ.* 342 (2024) 123340.
- [69] W. Liu, C. Song, M. Kou, Y. Wang, Y. Deng, T. Shimada, L. Ye, Fabrication of ultra-thin g-C<sub>3</sub>N<sub>4</sub> nanoplates for efficient visible-light photocatalytic H<sub>2</sub>O<sub>2</sub> production via two-electron oxygen reduction, *Chem. Eng. J.* 425 (2021) 130615.
- [70] H. Liang, A. Wang, R. Cheng, X. Tian, S. Jing, P. Tsiakaras, Efficient photocatalytic H<sub>2</sub>O<sub>2</sub> production ability of a novel graphitic carbon nitride/carbon composites under visible light, *Small* 19 (2023) 2303813.
- [71] Y. Yang, Z. Zeng, G. Zeng, D. Huang, R. Xiao, C. Zhang, C. Zhou, W. Xiong, W. Wang, M. Cheng, W. Xue, H. Guo, X. Tang, D. He, Ti<sub>3</sub>C<sub>2</sub> MXene/porous g-C<sub>3</sub>N<sub>4</sub> interfacial Schottky junction for boosting spatial charge separation in photocatalytic H<sub>2</sub>O<sub>2</sub> production, *Appl. Catal. B: Environ.* 258 (2019) 117956.